Spin correlations in $\vec{p}\vec{p} \to pn\pi^+$ pion production near threshold

W. W. Daehnick,* Swapan K. Saha,† and R. W. Flammang‡

Department of Physics and Astronomy, University of Pittsburgh, Pittsburgh, Pennsylvania 15260

H. O. Meyer, J. T. Balewski, R. E. Pollock, B. von Przewoski, T. Rinckel, P. Thörngren-Engblom,§ and A. Wellinghausen‖

Department of Physics and Cyclotron Facility, Indiana University, Bloomington, Indiana 47405

B. Lorentz,¶ F. Rathmann,¶ B. Schwartz, and T. Wise

University of Wisconsin-Madison, Madison, Wisconsin 53706

P. V. Pancella

Western Michigan University, Kalamazoo, Michigan 49008

A first measurement of longitudinal as well as transverse spin correlation coefficients for the reaction $\vec{p}\vec{p}$ $\to pn\pi^+$ is made using a polarized proton target and a polarized proton beam. We report complete measurements for this reaction at 325-, 350-, 375-, and 400-MeV beam energies. The spin coefficients $A_{xx}+A_{yy}$, $A_{xx}-A_{yy}$, A_{zz}, and A_{xz} and the analyzing power A_y, as well as angular for $\sigma(\theta_\pi)$ and the polarization observables $A_{ij}(\theta_\pi)$, are extracted. Partial wave cross sections for transition channels are obtained from a partial-wave analysis that included transitions with final-state momenta of $l \leq 1$. The measurements of the $\vec{p}\vec{p} \to pn\pi^+$ polarization observables are compared with the predictions from the Jülich meson exchange model. The agreement is very good at 325 MeV, but it deteriorates increasingly for the higher energies. At all energies agreement with the model is better than for the reaction $\vec{p}\vec{p} \to pp\pi^0$.

I. INTRODUCTION

Pion-nucleon interaction has provided increasingly sensitive tests of nuclear theory. One of the challenges yet to be met is to understand the polarization observables for pion production in $\vec{p}\vec{p}$ collisions. This is especially interesting near threshold, where few partial waves contribute and where calculations should be more manageable and more conclusive.

After the initial theoretical work in the 1950s by Gell-Mann and Watson [1] and Rosenfeld [2], more than a decade elapsed before explicit $pp \to pp\pi^0$ and $pp \to pn\pi^+$ cross sections for Ss ($l_{NN}=0$, $l_\pi=0$) transitions were predicted by Koltun and Reitan [3] in 1966 and by Schillaci, Silbar, and Young [4] in 1969. When the small cross sections very close to threshold could finally be measured 20 years later [5,6], it turned out that these calculations had missed the true cross sections by factors up to 5. This realization spurred much new theoretical research.

To date the Jülich meson exchange model [7–11] has yielded the most successful calculations. This model represents a much advanced development of the approach of Ref. [3] and builds on the insights of the 1990s (e.g., those of Lee and Riska [12] and many others). It permits detailed calculations beyond $l_\pi=0$ transitions, and provides analyzing powers and spin correlation coefficients for the near-threshold region. The Jülich model incorporates all the basic diagrams: realistic final-state interactions, off-shell effects, contributions from the delta resonance, and the exchange of heavier mesons. With the exception of the heavy meson exchange term there are no adjustable parameters. At this time it is the only model with predictions that can be compared to our measurements. However, the Jülich model does not account for quark degrees of freedom, the potential study of which had motivated our experiment initially.

Ideally, one would interpret the basic pion production reactions in a framework compatible with QCD, e.g., calculations using chiral perturbation theory (χPT). However, with one exception [13], the χPT calculations published to date are still restricted to $l_\pi=0$. Moreover, for all three $pp \to X\pi$ reactions, the χPT cross sections remain a factor of or more below experiment [14]. This shortcoming may attributable to the difficulties of χPT for momentum transfers larger than m_π. The χPT calculations published to are best viewed as works in progress [15]

Calculations and experiments very close to threshold require great care. For Ss transitions ($l_\pi=0$, $l_{pn}=0$) in $pp \to pn\pi^+$ only one amplitude is calculated, and the dependence is trivial. However, the near-threshold cross sec-

─────────

*Email address: daehnick@pitt.edu

†Permanent address: Bose Institute, Calcutta 700009, India.

‡Present address: Westinghouse Nuclear, Pittsburgh, Pennsylvania.

§Present address: Department of Radiation Science, Uppsala, Sweden.

‖Email address: arne.wellinghausen@gmx.net

¶Present address: Institut für Kernphysik, Forschungszentrum Jülich, 52425 Jülich, Germany.

tion and its energy dependence are significantly modified by "secondary" effects, such as final-state interactions that are particularly important for $l_{pn}=0$.

Measurements very close to threshold can present difficulties because the cross sections are small, of the order of 1 μb, and change rapidly with energy. The energy of the interacting nucleons for reactions very close to threshold must be precisely known and maintained. At the Indiana University Cyclotron Facility (IUCF) this was accomplished by the use of a very thin internal target and the precise beam energy control of the Cooler (storage) Ring. The IUCF Cooler also generates a low background.

The earliest studies of $pp \rightarrow pn\pi^+$ very close to threshold [6,16–18] had available a stored IUCF beam of $\leqslant 50$ μA. They used an unpolarized gas jet target and measured cross sections and analyzing powers from 293 MeV (i.e., 0.7 MeV above the π^+ production threshold) to 330 MeV. These experiments deduced cross sections for Ss pion production very close to threshold. As long as Ss production of pions strongly dominated, analyzing powers also provided information for Sp ($l_\pi = 1$) admixtures [18]. At 325 MeV and above, higher partial waves enter significantly, but the larger cross sections make it practical to explore analyzing powers and spin correlation coefficients, which allow a much more detailed comparison of theory and experiment. At the upgraded IUCF Cooler Ring, an intense polarized proton beam with a large longitudinal component and an efficient windowless polarized hydrogen target now permit measurements of all spin correlations coefficients for $\vec{p}\vec{p} \rightarrow pn\pi^+$. Some initial results for transverse spin correlations were reported in Ref. [19].

The goal of the present study is to quantify the growing importance of higher partial waves (Sp, Ps, Pp, and, potentially, Sd transitions) by measuring analyzing powers and spin correlation coefficients as a function of energy. These polarization observables are sensitive indicators of the reaction mechanism and the contributing partial waves [18,20,21], and are a powerful tool in determining transition amplitudes empirically. In this experiment we measured $A_{xx} + A_{yy}$, $A_{xx} - A_{yy}$, A_{zz}, A_{xz}, as well as the polarization observables A_y and A_z for the energy region 325–400 MeV.

II. EXPERIMENT

A. Experimental considerations

The Cooler Ring of the IUCF produces protons of energies up to 500 MeV, with polarization of $P \approx 0.65$, low emittance, and low background. This permits in-beam experiments of reactions with microbarn cross sections. The improvement of beam intensity at the IUCF over time now allows the use of very thin polarized targets. During the $\vec{p}\vec{p} \rightarrow pn\pi^+$ experiment typical intensities of the stored polarized beam ranged from 100 to 300 μA.

The apparatus for polarized internal target experiments (PINTEX) makes use of a windowless target cell continuously filled by a polarized atomic hydrogen beam. The measurements cycle through a full set of relative beam and target spin alignments. The technical aspects of beam preparation,

electronics, and target and detector properties were reported previously in Ref. [22]. As is customary, the beam is defined to travel in the positive z direction, y is vertical, and x completes a right-handed coordinate system. Below is a brief review of parameters pertinent to the data analysis.

In the experiment we used the Madison atomic beam target with a storage cell of very low mass [23,24]. The storage cell had a length of 25 cm and a diameter of 1.2 cm. This open-ended cylindrical cell produces a triangular shape of the target density distribution with its maximum at the center ($z=0$). It was made of a thin (25 μm) aluminum foil to keep background events caused by the beam halo to a minimum. A Teflon coating was used to inhibit depolarization of the target atoms. Sets of orthogonal holding coils surround the storage cell. The coils are used to align the polarized hydrogen atoms in the $\pm x$, $\pm y$, and $\pm z$ directions. Typical target polarizations were $Q=0.75$, and the approximate target density was 1.4×10^{13} atoms/cm^2.

The target spin alignment can be changed in less than 10 ms. During runs the target polarization direction was changed every 2 sec, and followed the sequence $\pm x$, $\pm y$, and $\pm z$. Each data-taking cycle had a constant beam polarization, and was set to last 5–8 min, after which the remaining beam was discarded. The beam polarization was reversed with each new cycle to minimize the effect of apparatus asymmetries. In the first phase of the experiment (run a) the beam spin directions were alternated between $+y$ and $-y$. In the more recent runs (b) solenoid spin rotators were used to give the beam spin a large longitudinal component. This spin rotation was energy dependent and produced roughly equal longitudinal (z) and vertical (y) spin components and a very small component in the (x) direction, as shown in Table I.

Elastic $\vec{p}\vec{p}$ scattering was used to measure and monitor the three beam polarization components as well as the luminosity. Elastic protons were detected with four plastic scintillators mounted at $\theta = 45°$, with $\phi = \pm 45°$ and $\pm 135°$. Coincident protons striking these monitor detectors (labeled S in Fig. 1) pass through wire chamber 1, so the needed tracking information is available. The product PQ of beam polarization (P) and target polarization (Q) was deduced from the large known spin correlation $A_{xx} - A_{yy}$ in elastic scattering [25]. A three-dimensional sketch of the detector system is shown in Fig. 1.

The reaction pions in this study had lab energies from 0.1 to 120.5 MeV, and were emitted at polar lab angles from 0° to 180°. By contrast, the reaction nucleons remain constrained by kinematics to forward angles below 31.2° and to lab energies from 20.8 to 227.9 MeV. This range of angles and energies affects the choice of detectors that can be employed. If both outgoing nucleons are protons as in $\vec{p}\vec{p} \rightarrow pp\pi^0$, one can ignore the pion and use a moderate size forward detector to intercept almost all ejectiles of interest [22]. This procedure was used for the simultaneously measured $\vec{p}\vec{p} \rightarrow pp\pi^0$ reaction [26]. The corresponding procedure for $\vec{p}\vec{p} \rightarrow pn\pi^+$ is to mount a large area neutron hodoscope behind the proton detectors, and determine the energies of the detected neutrons by time of flight. The con-

TABLE I. Beam energies, integrated luminosities for the $p+\pi^+$ measurements, and the products of beam and target polarization for runs a and b. (No $p+n$ data were taken in run a. The $p+n$ measurements began in the middle of run b and have correspondingly lower integrated luminosities.)

Energy (MeV)	Run a		Run b			
	$\int Ldt$ (nb^{-1})	$P_y Q$	$\int Ldt$ (nb^{-1})	$P_x Q$	$P_y Q$	$P_z Q$
325.6	2.163	0.456±0.003	3.0	0.059±0.002	0.333±0.002	0.296±0.003
350.5	0.901	0.342±0.004	1.3	0.053±0.003	0.316±0.003	0.267±0.005
375.0	3.024	0.514±0.004	4.1	0.041±0.002	0.333±0.002	0.266±0.004
400.0	0.831	0.526±0.006	1.1	0.039±0.004	0.289±0.004	0.203±0.008

struction and operation of the neutron hodoscope were described previously in Ref. [27].

All detectors are segmented because the energies of the coincident reaction particles need to be measured independently. Monte Carlo calculations suggest that eight $\Delta\phi$ segments are sufficient, because of the tendency of the ejectiles to have significantly different azimuthal angles. The K detector was needed to obtain the necessary stopping power for the more energetic pions and protons. Identification of the charged particles was usually accomplished by their time of flight vs energy correlation, where the start signal was supplied by the F detector and the stop signal was provided by the E detector. The pion and proton distributions were generally well separated. Figure 2 shows a typical particle ID spectrum for accepted $p\pi^+$ coincidence events.

The more energetic ejectiles stop in the K detector. Superior particle identification is obtained by comparing the energies deposited in the K vs E detectors, as seen in Fig. 3.

We measured the polarization observables A_{ij} in two different ways: (1) by measuring the pions directly, in coincidence with protons (the $p+\pi$ method), and (2) by reconstructing pion momenta from the measured proton and neutron momenta (the $p+n$ method). The first method had the advantage of simplicity and a high count rate, but we cannot measure pions at large angles due to the limited detector size. Therefore, the spin-dependent cross-section ratios could be compared with theoretical spin correlation coefficients only at forward angles. The second method is free from this limitation, but at the cost of the low neutron detection efficiency and therefore much lower statistics.

B. Measurement of $p+\pi^+$ coincidences

We accept events with two charged reaction particles (p and π^+) in coincidence. They must show separate tracks in the wire chambers WC1 and WC2, trigger separate sections of the E detectors, and at least one section of the F detector, but not the scintillator (V) veto. The trajectories of the protons and pions are deduced from the wire chamber position readings. Their angular resolution was limited primarily by multiple scattering in the 1.5-mm-thick F detector and in the 0.18-mm-thick stainless-steel exit foil. Approximate angular resolutions (in the lab system) are $\sigma=0.5°$ for protons and $1°$ for pions. This resolution was fully sufficient for the angular variations expected.
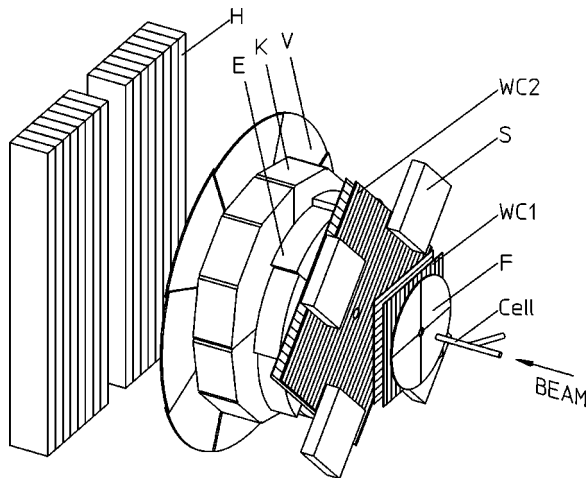

FIG. 1. The PINTEX detector for the experiment: F is a thin timing detector. S labels one of the four detectors for the elastic pp scattering monitor. WC1 and WC2 are wire chambers. E and K are segmented plastic scintillator stacks that determine the energy of the charged reaction products. V is the charged particle veto detector, and H is the neutron hodoscope.
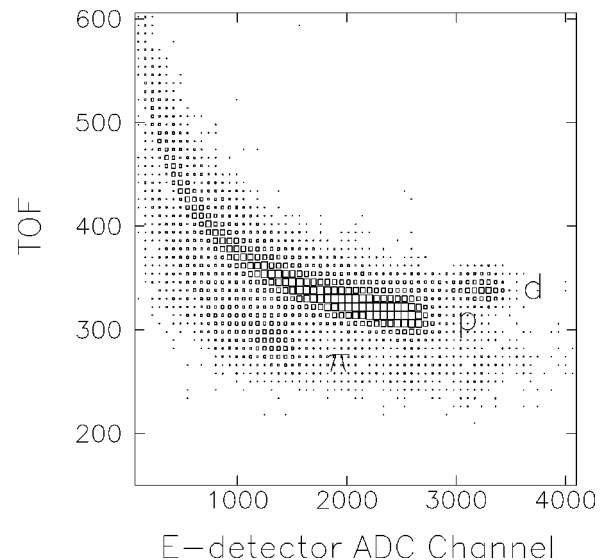

FIG. 2. Raw ejectile time of flight (channels) vs energy deposited in the E detector by pions, protons, and deuterons. Triggers from two charged particles tracks and (no K) were a prerequisite. This spectrum was used for identification of protons and pions.
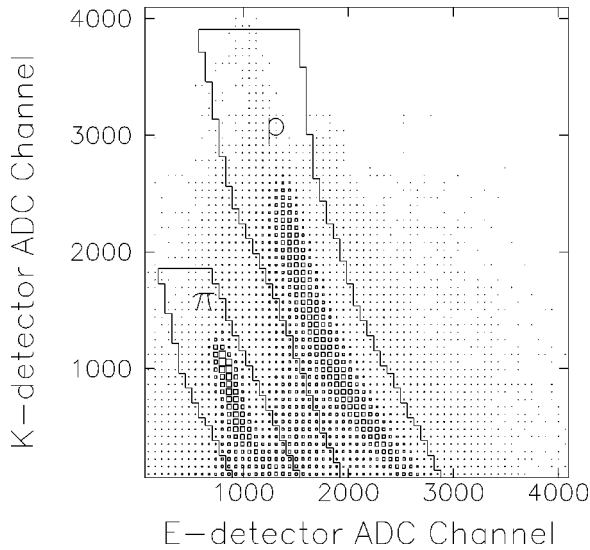
FIG. 3. Particle identification cuts at 375 MeV for energetic ejectiles based on energy deposited in the K detector as a function of energy loss in the E detector. Acceptable events had to be inside the regions outlined.

The good intrinsic angular resolution of the wire chambers was used to check the consistency of the pion and neutron position readouts by tracing elastic protons to the hodoscope bars, and comparing predicted and observed position readings. It was found that from run to run the beam axis and the detector symmetry axis could differ slightly in direction and also in their relative x and y coordinates at $z=0$ (the target center). We could also cross check the nominal z separation of the wire chambers, since the separation and location of the hodoscope bars was fixed and well known. Small corrections of 1–3 mm had to be applied in software to the detector positions. After such corrections the remaining systematic angular error of the measured polar angles is about $0.04°$.

Charged particles that do not stop in or before the K detector trigger the V detector and are tagged as likely elastic events and generally vetoed. At 400 MeV we reach the design limit of the charged-particle detectors, and the veto detector begins to see (and reject) the most energetic pions at small angles. In deducing the energy spectra account was taken of the differing nonlinearity of light production for protons and pions by the plastic scintillators, as well as of energy losses in the exit foil, the F detector, air, and other materials between the scintillators. After calibrations of all detector segments the detector stack provided an energy resolution for typical reaction protons and pions of about $\Delta E/E = 0.09$ [full width at half maximum (FWHM)]. The missing mass spectra contain a background continuum (see Fig. 4), which at higher beam energies stretches slightly beyond the missing mass peak.

The trajectory traceback indicates that this background is primarily caused by beam halo hitting the Al and teflon components of the target cell. Without a target gas (and the beam heating normally produced by it) almost no background is seen. In order to obtain a realistic background shape near and below the missing mass peak, the target cell was filled with
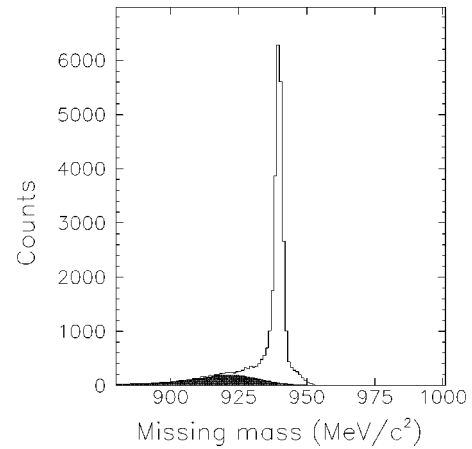

FIG. 4. Neutron missing mass reconstructed from measured pion and proton momenta. The background spectrum shown (dark area) results if the atomic hydrogen in the target cell is replaced by nitrogen gas.

N_2. This gas will produce some background of its own, but just as importantly it heats the circulating beam (as the hydrogen gas would) and reproduces the ordinary beam halo. We found that the "N_2 spectra" "seen" after the common software cuts looked identical to the background "tail" in the hydrogen missing mass spectra. Therefore, N_2 spectra were measured with good statistics, and their shape was later used to correct for background under the missing mass peak. Our statistically most accurate measurements were obtained in the $p+\pi$ mode, i.e., by observing pions and protons in coincidence.

C. Measurement of $p+n$ coincidences

Reaction neutrons in coincidence with protons were detected in a large hodoscope consisting of 16 long plastic scintillator bars. The bars were placed symmetrically about the beam direction in a plane defined by $z=1.48$ m. They were 15 cm deep, and mounted so that their dimension in the y and x directions were 120 and 5 cm, respectively (see Fig. 1). The position in the y direction was determined from the differing arrival times of the scintillator light pulses read out by the top and bottom photomultipliers. The y-position resolution was $\sigma \approx 1.7$ cm. At 325 MeV the geometric acceptance for $p+n$ detection is comparable to that for the $pp \rightarrow pp\pi^0$ branch; however, the achievable event detection rate is much smaller because of the low neutron detection efficiency. The neutron pulse height threshold was set as low as practical, and corresponds to 5-MeV electrons for all bars. At this threshold a 15-cm-thick plastic scintillator averages a neutron detection efficiency of about 0.17 for the neutron energies of this experiment [27].

A thicker neutron detector would be more efficient, but along with technical problems it would produce a correspondingly poorer time of flight resolution, since the length of the available flight path was limited to 1.5 m. In this experiment an additional reduction of the neutron detection efficiency arose because the E and K proton detectors are located in front of the neutron hodoscope, and represent a

26-cm-thick (polystyrene) absorber for the reaction neutrons. Resulting neutron losses in this "absorber" range from 30% for the highest energy neutrons to about 90% for those at the very lowest energies. As a consequence the energy-averaged effective neutron detection efficiency was reduced to a value of about 0.07. Since neutron energies are measured and neutron reaction cross sections are known [28], corrections for energy-dependent efficiency losses can and have been made, but the loss in the counting rate seriously limited the statistics obtained.

The neutron energy was measured by neutron time of flight. In applying this method we use the correlated proton trigger from $\vec{p}\vec{p} \rightarrow pn\pi^+$ in the F detector. Since the proton arrival at the F detector is delayed, one has to use a two-step process: First, the trigger time difference (F detector time minus hodoscope mean time) is measured. Next the timing must be corrected for the proton flight time to the F detector, since the F detector is triggered by the proton after it has traveled about 30 cm before reaching the F detector. This correction is based on the measured proton energy and reconstructed track length. Neutron times of flight (TOF's) range from 5 to 12 ns.

The dominant contribution to the TOF resolution comes from the 15-cm bar thickness, which constitutes 10% of the flight path and cannot be overcome with the available detectors. Smaller contributions come from the intrinsic timing resolution of the hodoscope (0.4-ns FWHM) and the F detector (0.5-ns FWHM, after amplitude walk correction). We note that the raw time resolution of the F detector is worse than the figure quoted above because of the trigger walk in the electronics and because of the light loss and travel delay of light from parts of the large four-section F detector more distant from the photomultipliers. A substantial improvement was achieved by employing a pulse height compensation function. Overall, we see a neutron time of flight resolution with $\Delta T/T \approx 0.1$. Therefore, the missing mass (MM) peak for π^+ from $p+n$ detection is not as sharp as for the corresponding neutron missing mass derived from $p+\pi^+$ events.

III. ANALYSIS

A. Monte Carlo simulations

Our Monte Carlo (MC) simulations of the experiment used the event generator GENBOD of the CERN library. The simulation was used to determine various limiting effects of the apparatus, and to derive corresponding corrections. The code contained the detailed geometry of the detector systems and the density distribution of the gas target. In the MC simulation we took into account the loss of energy of the charged particles before entering the detectors, detector resolutions, charged particle multiple scattering, pion decay in flight, energy-dependent neutron detection efficiency and the probability of nuclear reactions of the reaction neutrons in the E and K detectors. In the MC simulation we have used a pn final-state interaction (FSI) based on the Watson-Migdal theory, and the equations were derived following Morton [29]. We found that at the lower energies the FSI has a large effect on the overall coincidence acceptance. The simulation
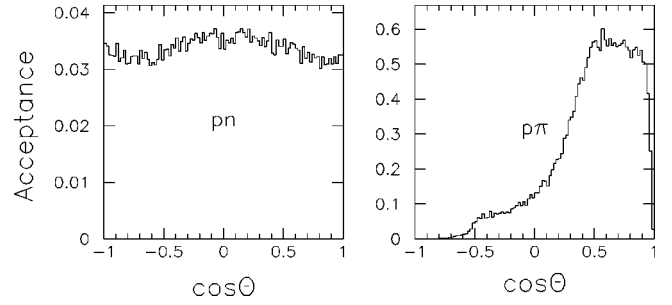

FIG. 5. Monte Carlo simulation for (a) $p+n$ and (b) the $p+\pi^+$ acceptances, in the center of mass system. The partial acceptance for pions seen in the $p\pi$ diagram at $\theta_\pi \gtrsim 70°$ results from the dominating forward boost for low energy pions. The cutoff at $\cos \theta_\pi \approx -0.5$ is caused by detector thresholds for the lowest ejectile energies.

also provided a guide to the expected energy and angular distribution of the reaction products.

Pion counting losses caused by the limited detector depth are not large enough to be detectable in the shape of spectra; however, the Monte Carlo simulation shows that they must be considered. At 400 MeV the loss for pions is 14% because this fraction of the forward pions is too energetic to stop in the K detector. Only about 0.2% of the reaction protons penetrate past the K scintillators and are vetoed. The loss of high-energy pions at small lab angles may create a small distortion of the 400 MeV $p+\pi$ data. Corrections to the 400-MeV spectra were not made since they would have to be very model dependent. We note parenthetically that the 400-MeV data from $p+n$ coincidences do not have this systematic error, but within statistics they agree with overlapping $p+\pi^+$ results. No "veto" losses are seen at 375 MeV or below.

The finite size of the individual detector segments produces some counting losses, since two sections have to trigger for acceptable events. However, systematic effects for the polarization observables are unlikely since the protons have no strong ϕ correlations with the pions. The segmentation used leads to a loss of about 7% in counting statistics for the $p+\pi^+$ branch. There is no such loss for $p+n$ detection. The charged particle detectors cover polar angles between 5° and 40° in the laboratory frame. Hence a large number of pions miss the detector. The total $p+\pi^+$ coincidence acceptance ranges from 21% at 325 MeV to 15% at 400 MeV.

For $p+n$ detection the MC simulation shows that the acceptance is symmetric about 90° although not quite isotropic. [See Fig. 5(a)]. Acceptance losses for $p+n$ coincidences attributable to the detector geometry alone are of the order of 25%. The major cause is the central hole in the proton detectors. After all geometric acceptance losses and detector inefficiencies for neutron detection are taken into account, the computed overall detection efficiency for pn coincidence events is 3.5%. It is seen in Fig. 5(a) that the angular variations of the coincidence efficiency for the reconstructed pion are small. This is so despite the fact that we cannot detect protons at angles $\leq 5°$ and neutrons at angles $\leq 2.5°$, and have reduced coverage by the hodoscope of some azimuthal angles for large neutron polar angles. The Monte Carlo ac-

ceptance curves for $p+n$ detection suggest that within the statistical accuracy of the experiment the spin-correlation parameters integrated over θ_π and ϕ_π would need no significant correction. Figure 5(b) shows the Monte Carlo simulation for $p\pi^+$ acceptance as a function of $\cos\theta_\pi$. For $p\pi^+$ coincidences the apparatus acceptance is only useful for $\theta_\pi \leqslant 70°$. Therefore, the integrated spin correlation coefficients will be deduced from the combined sets of the $p+\pi^+$ and $p+n$ coincidences.

B. Analysis of $p+\pi^+$ coincidences

The energies of the charged particles are measured by the plastic scintillator systems E and K. The calculated momenta of the unobserved particles strongly depend on the energies of the detected ejectiles, so considerable attention was given to a careful energy calibration of all detectors. The complex geometry of the segmented plastic detectors required corrections for light collection that primarily were derived from the observation of elastically scattered protons. An xy-position correction factor was applied to account for this dependence. A second pulse height correction factor was applied to compensate for a variation of phototube gains with the orientation of the magnetic guide field for the target polarization. For details see Ref. [22].

The corrected pulse heights L were converted into the deposited energy E using

$$E = L + k_1 \sqrt{L} + k_0. \qquad (1)$$

The nonlinear term corrects for light quenching in plastic scintillators. k_0 and k_1 are calibration constants. L is the sum of the light pulse from the E and K detectors in MeV, and is given by $L = c_1(E_{light} + c_2 K_{light} + c_3)$. The constants c_1, c_2, and c_3 are gain matching constants, and E_{light} and K_{light} correspond to the observed light pulses in the E and K detectors, respectively. The constant c_3 corrects for small energy losses in the material between the E and K detectors. It is small and set equal to zero when there is no K trigger.

The total kinetic energy of the charged particle was calculated by also taking account of the energy lost by the charged particle on its way to the E detector. The calibration constants were fine tuned by utilizing kinematical relations. We required that the missing mass centroid was at its predicted value and that the angular distribution of the pions from the simultaneous measurement of the reaction $\vec{p}\vec{p} \rightarrow pp\pi^0$ was symmetric in the center-of-mass (c.m.) system about $\theta_\pi = 90^0$. This symmetry was sensitive to the relative size of the calibration coefficients. However, the variation of the deduced spin correlation coefficients under different reasonable combinations of the calibration constants was small and less than the statistical errors.

Figure 6 shows the directly observed π^+ differential cross sections plotted against $\cos\theta_\pi$ in the c.m. coordinate system. We note that there are almost no counts for pion back angles $-1 < \cos\theta_\pi < 0$, as expected from the apparatus acceptance [compare Fig. 5(b)].

Figure 7 shows missing mass spectra seen at 325 MeV for four combinations of vertical beam and target polarization at
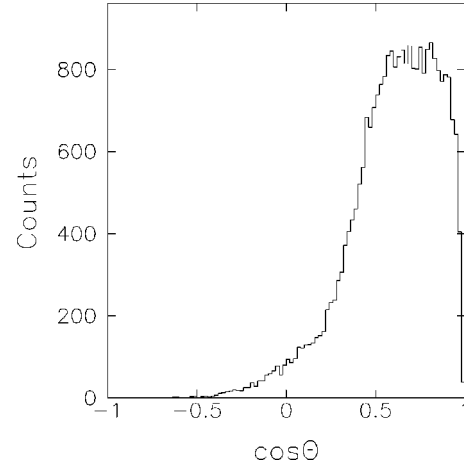

FIG. 6. Detected pions at 325 MeV as a function of θ_π. Only events with $\cos\theta_\pi \geqslant 0.4$ were used for the analysis.

equal integrated luminosity. The polarization observables are obtained from the ratio of "yields" for different spin orientations. The yields to be used are the integrated counts inside the missing mass gates minus background. In order to estimate the error from uncertainties in the background we varied the background subtraction by $\pm 25\%$. The effect on the final results was smaller than the statistical error. At 325 MeV the off-line resolution of the neutron missing mass peak was $\sigma = 1.4$ MeV/c^2. Even before software cuts and background correction it is apparent from Fig. 7 that different spin combinations produce very different yields.

It turns out that the decay in flight of pions plays a negligible role for these data. It will appreciably affect only the (undetected) backward scattered pions as these have much
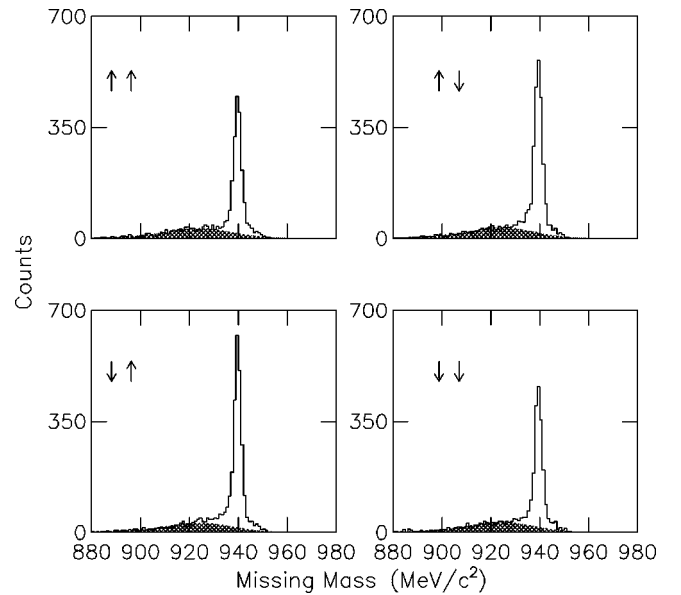

FIG. 7. Distributions of the calculated missing mass m_x for $p + \pi^+$ detection at 325-MeV bombarding energy, for the four combinations of vertical beam and target polarization. A sharp peak (≈ 3.5-MeV/c^2 FWHM) is seen at 939.6 MeV/c^2, the neutron rest mass. The shaded region indicates the background distribution.
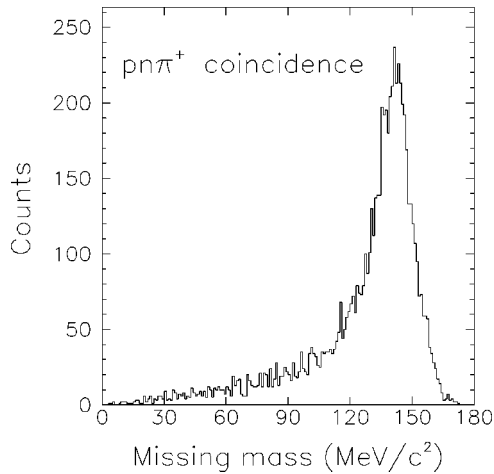
FIG. 8. Missing mass spectrum for $pn\pi^+$ triple coincidences, based on the measured neutron and proton energies. This spectrum contains no background from any competing reaction. The missing mass tail here is a consequence of some inaccurately measured neutron momenta. See the text.

lower lab energies than the forward pions. For the final analysis we selected the $pp\to pn\pi^+$ events of interest by using a gate of 30 MeV or wider over the relevant missing mass peak. Gates as narrow as 10 MeV did not produce systematic changes, and neither did they measurably reduce background induced errors. However, the narrower gates lead to some loss of statistics.

C. Analysis of $p+n$ coincidences

This detection channel has the advantage that the acceptance for the detection of $p+n$ coincidences has little angular variation. So θ_π- and ϕ-dependent acceptance corrections generally can be ignored. Therefore, the $p+n$ coincidences importantly complement the $p+\pi^+$ channel. Reliance on $p+n$ angular distributions at large angles leads to larger statistical error bars relative to the $p+\pi^+$ (forward) region. However, the combination of the two detection modes provides data for the full angular range, and so keeps the integrated spin correlation coefficients model independent.

In the $p+n$ analysis we first analyzed only those events where all three reaction particles (p, n, and π^+) were detected (the triple coincidence). Next we evaluated the case where the pions missed the E detector, but a proton and a neutron were detected (double coincidence). The energy of reaction protons was determined using the calibration constants described above. The energy of the neutrons was determined by measuring their TOF to the hodoscope. The MC simulation showed that, although the F detector was always triggered by protons for a $p+n$ double coincidence, in the case of a $pn\pi^+$ triple coincidence it was triggered by the faster pions. Therefore, depending on the event class, we corrected the neutron TOF by adding the time it takes either for the coincident proton or the pion to reach the F detector. A calculated offset was added to the timing signal of each hodoscope bar in order to make the timing information independent of the bar electronics. This correction was obtained

by calibrating the timing circuits with elastic proton scattering.

For $\theta_{\pi,lab}\leqslant40°$ we observe $pn\pi^+$ triple coincidences, which are practically free of background. (The absence of accepted events from the N_2 gas target showed that the triple $pn\pi^+$ hardware coincidence under standard software conditions eliminates all background from the target wall and target impurities.) These events proved very valuable in assessing the correct shape of the missing mass peaks in $p+n$ and $p+\pi$ events. If a missing mass spectrum for triple coincidences is calculated based on the pion and proton momenta the (neutron) missing mass spectrum shows a very sharp peak as in Fig. 4, but there is no "background tail" at all. The triple coincidence spectrum confirms the background subtraction shown in Figs. 4 and 7.

If the same triple coincidence events are used to calculate the (pion) missing mass by using the proton and neutron momenta (i.e., ignoring the simultaneously known pion momenta) we obtain the spectrum shown in Fig. 8. This spectrum can be used as a standard for the missing mass that $p+n$ (double coincidence) events would have in the absence of background.

The MM distribution peaks at the true pion mass of 139.6 MeV, but there also is a "tail" over a wide range of the missing mass spectrum which is not background related. We conclude that the counts in the MM tail of Fig. 8 represent genuine $pn\pi^+$ events from the hydrogen target, albeit events with poorly determined neutron momenta. We estimate that up to 20% of the $p+n$ coincidences contain neutron observables that are distorted by interactions of neutrons with the K or E detectors. That is, neutrons can undergo small angle elastic and inelastic scatterings, but still reach the hodoscope. This would lead to incorrect readings for polar and azimuthal neutron angles and hence to an incorrect missing mass calculation.

Such events with poorly determined missing masses were excluded from further analysis. For all $p+n$ events we reduce genuine background and avoid analyzing measurably distorted $p+n$ events by using a missing mass gate from 100 to 160 MeV.

Using the triple coincidence MM spectrum as a standard, the background under the missing mass peak for two-particle $p+n$ coincidences was deduced by adding a fraction of the measured unstructured N_2 background continuum to the "standard" MM spectrum until the observed $p+n$ MM spectrum shape was reproduced. The tail in the latter is flatter and more pronounced because of actual background contributions. To estimate the error in this procedure we varied the match until it became unrealistic ($\pm15\%$). A typical missing mass spectrum for $p+n$ (double coincidence) detection is shown in Fig. 9. In the final result the uncertainty from this background subtraction was about half as large as the statistical error.

At 375 MeV the resolution of the pion MM peak was $\sigma=9$ MeV/c^2. Pion angular and energy distributions from $p+n$ detection were computed using only events inside this missing mass gate. Some resulting distributions are compared with Monte Carlo projections for the laboratory coordinate system in Fig. 10. The end points of these distribu-
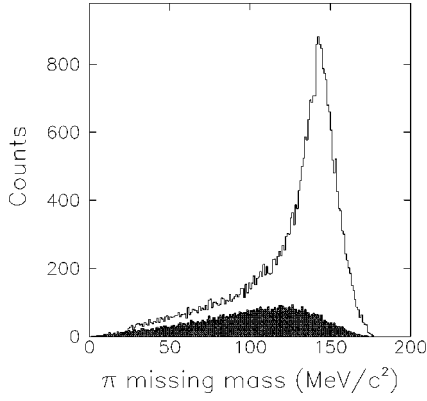
FIG. 9. The π^+ missing mass (m_x) spectrum at 375 MeV calculated from the measured neutron and proton momenta. The deduced background is shown by the lower distribution. For the analysis, events with $100 \leqslant m_x \leqslant 160$ were accepted.

tions agree well with the kinematics of the experiment as they must. The solid curves represent pure $l_\pi = 0$ MC calculations. Although $l_\pi = 0$ makes the major contribution, this MC assumption produces oversimplified energy and angular distributions. Nevertheless, the simulated distributions agree reasonably well with the data.

Figure 11 shows the deduced pion angular distribution in the center-of-mass system. The reconstructed π^+ distribution is plotted against $\cos \theta_\pi$ in the center of mass [corrected for background and for the slightly nonuniform acceptance shown in Fig. 5(a)]. As expected, it is nonisotropic and symmetric about $\theta_\pi = 90°$ within statistical errors.

IV. POLARIZATION OBSERVABLES

A. Formalism for spin correlation coefficients

The meaning of the symbols A_{ij} used for polarization observables is defined by Eq. (2). In terms of the "Cartesian polarization observables" the spin-dependent cross section is written as
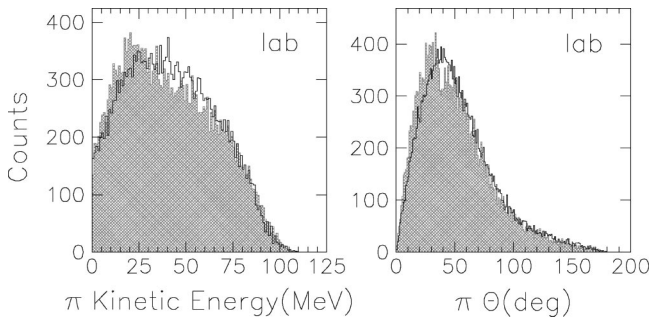

FIG. 10. Energy and angular distributions for $p + n$ coincidences at 375 MeV, compared with Monte Carlo projections (solid lines) in the laboratory system. Agreement is expected for the kinematic limits. However, the distributions may differ because the $l_\pi = 0$ assumption for the MC simulation is an oversimplification at and above 325 MeV.
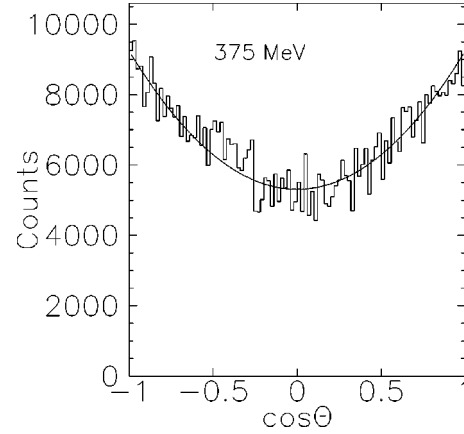

FIG. 11. The relative π^+ production cross section $\sigma_0(\cos \theta_\pi)$ at 375 MeV as deduced from $p + n$ coincidences.

$$\sigma(\xi, \vec{P}, \vec{Q}) = \sigma_0(\xi)\left[1 + \sum_i P_i A_{i0}(\xi) + \sum_j Q_j A_{0j}(\xi) \right.$$
$$\left. + \sum_{i,j} P_i Q_j A_{ij}(\xi) \right], \tag{2}$$

where ξ stands for the pion coordinates θ_π and φ_π, the energy defining pion momentum p_π, and the proton coordinates θ_p and φ_p. The unpolarized cross section is $\sigma_0(\xi)$, and the polarization of the beam and the target is denoted by the vectors $\vec{P} = (P_x, P_y, P_z)$ and $\vec{Q} = (Q_x, Q_y, Q_z)$. The subscripts i and j stand for x, y, or z, and the sums extend over all possibilities. The resulting 15 polarization observables include the beam analyzing powers A_{i0}, the target analyzing powers A_{0j}, and the spin correlation coefficients A_{ij}.

The partial wave analysis for $\vec{p}\vec{p} \to pn\pi^+$ is similar to that for $\vec{p}\vec{p} \to pp\pi^0$ in terms of transition amplitudes. However, the $pp \to pn\pi^+$ transitions have isoscaler as well as isovector components. The different isospins in $\vec{p}\vec{p} \to pn\pi^+$ modify the selection rules for the reaction, and lead to polarization observables that are different. The general relations between reaction amplitudes and angular distributions, however, remain almost identical. The applicable partial wave formalism was discussed in detail in Ref. [26]. We use the same notation as in Ref. [26], and reiterate some relevant definitions and theoretical relations below. Several names are in use for polarization observables. Their meaning is as defined below:

$$A_\Sigma(\xi) \equiv A_{xx}(\xi) + A_{yy}(\xi), \tag{3a}$$

$$A_\Delta(\xi) \equiv A_{xx}(\xi) - A_{yy}(\xi), \tag{3b}$$

$$A_\Xi(\xi) \equiv A_{xy}(\xi) - A_{yx}(\xi). \tag{3c}$$

For identical particles in the entrance channel there are seven independent polarization observables:

$$A_{y0}(\xi), \quad A_\Sigma(\xi), \quad A_{zz}(\xi), \quad A_{xz}(\xi), \quad A_\Delta(\xi),$$

$$A_\Xi(\xi), \quad A_{z0}(\xi). \tag{4}$$

This paper addresses the first five observables of this set. The remaining two, $A_\Xi(\xi)$ and $A_{z0}(\xi)$, can be nonzero only for noncoplanar final states. In the following we will integrate over the angles of the nucleon, and thus these two observables vanish if parity is conserved.

It is common to display the bombarding energy dependence of the observables in terms of the dimensionless parameter η, which is defined as

$$\eta = p_{\pi,max}/m_{\pi^+}. \tag{5}$$

The term ''near threshold'' is meant to include the energy region with $\eta < 1$, i.e., below 400 MeV. Setting $c = \hbar = 1$, the maximum value of the π^+ momentum is found from

$$p_{\pi,max} = \frac{1}{2\sqrt{s}}\sqrt{\{[s-(m_n+m_p+m_{\pi^+})^2][s-(m_n+m_p-m_{\pi^+})^2]\}}, \tag{6}$$

where $\sqrt{s}$ is the total center-of-mass energy, and m_p, m_n, and m_{π^+} are the masses of the proton, neutron, and pion, respectively. (We explicitly labeled the pion as π^+ to emphasize that the π^+ and π^0 mass difference matters here.)

Below we quote some useful relations between integrated spin correlation coefficients and some directly observable spin dependent cross sections. For two colliding spin-1/2 particles, one can define three total cross sections, two of which depend on the spin. The total cross sections are related to the observables above by

$$\sigma_{tot} = \int \sigma_0(\xi)d\Omega_p d\Omega_\pi dp_\pi, \tag{7a}$$

$$\Delta\sigma_T = -\int \sigma_0(\xi)A_\Sigma(\xi)d\Omega_p d\Omega_\pi dp_\pi, \tag{7b}$$

$$\Delta\sigma_L = -2\int \sigma_0(\xi)A_{zz}(\xi)d\Omega_p d\Omega_\pi dp_\pi. \tag{7c}$$

Here $d\Omega = d\cos\theta\, d\varphi$, and the integration extends over $0 \leqslant \theta \leqslant \pi$, and all pion momenta. $\Delta\sigma_L/\sigma_{tot}$ and $\Delta\sigma_T/\sigma_{tot}$ can have values between -2 and $+2$.

The integrated spin correlation coefficients are defined as

$$\overline{A_\Sigma} = \left[\int \sigma_0(\xi)A_\Sigma(\xi)d\Omega_p d\Omega_\pi dp_\pi\right]\bigg/ \sigma_{tot}, \tag{8a}$$

$$\overline{A_{zz}} = \left[\int \sigma_0(\xi)A_{zz}(\xi)d\Omega_p d\Omega_\pi dp_\pi\right]\bigg/ \sigma_{tot}, \tag{8b}$$

$$\overline{A_\Delta} = \left[\int \sigma_0(\theta_\pi)A_\Delta(\theta_\pi)\sin\theta_\pi d\theta_\pi\right]\bigg/ \sigma_{tot}, \tag{8c}$$

$$\overline{A_{xz}} = \left[\int \sigma_0(\theta_\pi)A_{xz}(\theta_\pi)\sin\theta_\pi d\theta_\pi\right]\bigg/ \sigma_{tot}, \tag{8d}$$

$$\overline{A_{y0}} = \left[\int \sigma_0(\theta_\pi)A_{y0}(\theta_\pi)\sin\theta_\pi d\theta_\pi\right]\bigg/ \sigma_{tot}. \tag{8e}$$

We note that $\overline{A_\Sigma}$ and $\overline{A_\Delta}$ differ by a scale factor from $\Delta\sigma_T$ and $\Delta\sigma_L$. These quantities can in principle be measured directly, although in this study they are derived from integration over $A_\Sigma(\cos\theta_\pi)$ and $A_{zz}(\cos\theta_\pi)$. The remaining three integrals must be defined differently. Here the spin correlations A_{ij} are taken at $\phi_\pi = 0$. (They cannot be integrated over the variable ϕ_π since they would vanish, as will be seen below).

Based on the dominance of Ss, Sp, Ps, and Pp transitions, general symmetries and spin coupling rules [26], the cross sections and spin correlation coefficients must have the general forms:

$$\sigma_0(\xi) = a_{00} + b_{00}(3\cos^2\theta_\pi - 1) + c_0(3\cos^2\theta_p - 1)$$
$$+ d_0(3\cos^2\theta_\pi - 1)(3\cos^2\theta_p - 1)$$
$$+ e_0\sin 2\theta_p\sin 2\theta_\pi\cos\Delta\varphi$$
$$+ f_0\sin^2\theta_p\sin^2\theta_\pi\cos 2\Delta\varphi, \tag{9a}$$

$$\sigma_0(\xi)A_{y0}(\xi) = [\{a_{y0} + b_{y0}(3\cos^2\theta_p - 1)\}\sin\theta_\pi$$
$$+ \{c_{y0} + d_{y0}(3\cos^2\theta_p - 1)\}\sin 2\theta_\pi]\cos\varphi_\pi$$
$$+ [e_{y0} + f_{y0}\cos\theta_\pi + g_{y0}(3\cos^2\theta_\pi - 1)]$$
$$\times \sin 2\theta_p\cos\varphi_p + [h_{y0}\sin\theta_\pi + i_{y0}\sin 2\theta_\pi]$$
$$\times \sin^2\theta_p\cos(2\varphi_p - \varphi_\pi)$$
$$+ j_{y0}\sin 2\theta_p\sin^2\theta_\pi\cos(2\varphi_\pi - \varphi_p), \tag{9b}$$

$$\sigma_0(\xi)A_\Sigma(\xi) = a_\Sigma + b_\Sigma(3\cos^2\theta_\pi - 1) + c_\Sigma(3\cos^2\theta_p - 1)$$
$$+ d_\Sigma(3\cos^2\theta_p - 1)(3\cos^2\theta_\pi - 1)$$
$$+ e_\Sigma\sin 2\theta_p\sin 2\theta_\pi\cos\Delta\varphi$$
$$+ f_\Sigma\sin^2\theta_p\sin^2\theta_\pi\cos 2\Delta\varphi, \tag{9c}$$

$$\sigma_0(\xi)A_{zz}(\xi) = a_{zz} + b_{zz}(3\cos^2\theta_\pi - 1) + c_{zz}(3\cos^2\theta_p - 1)$$
$$+ d_{zz}(3\cos^2\theta_p - 1)(3\cos^2\theta_\pi - 1)$$
$$+ e_{zz}\sin 2\theta_p\sin 2\theta_\pi\cos\Delta\varphi$$
$$+ f_{zz}\sin^2\theta_p\sin^2\theta_\pi\cos 2\Delta\varphi, \tag{9d}$$

$$\sigma_0(\xi)A_\Delta(\xi)=[a_\Delta+b_\Delta(3\cos^2\theta_p-1)]\sin^2\theta_\pi\cos 2\varphi_\pi$$
$$+[c_\Delta+d_\Delta(3\cos^2\theta_\pi-1)]\sin^2\theta_p\cos 2\varphi_p$$
$$+e_\Delta\sin 2\theta_p\sin 2\theta_\pi\cos(\varphi_p+\varphi_\pi), \tag{9e}$$

$$\sigma_0(\xi)A_{xz}(\xi)=[\{a_{xz}+b_{xz}(3\cos^2\theta_p-1)\}\sin\theta_\pi$$
$$+\{c_{xz}+d_{xz}(3\cos^2\theta_p-1)\}\sin 2\theta_\pi]\cos\varphi_\pi$$
$$+[e_{xz}+f_{xz}\cos\theta_\pi+g_{xz}(3\cos^2\theta_\pi-1)]$$
$$\times\sin 2\theta_p\cos\varphi_p+[h_{xz}\sin\theta_\pi+i_{xz}\sin 2\theta_\pi]$$
$$\times\sin^2\theta_p\cos(2\varphi_p-\varphi_\pi)$$
$$+j_{xz}\sin 2\theta_p\sin^2\theta_\pi\cos(2\varphi_\pi-\varphi_p). \tag{9f}$$

Here we have used the abbreviation $\Delta\varphi\equiv\varphi_p-\varphi_\pi$. Equations (9) explicitly depend on the four angles θ_p, φ_p, θ_π, and φ_π. The energy-dependent parameter p_π is contained in the coefficients. Statistics in this experiment are not sufficient to present double or higher differential cross sections. Therefore, we integrate over the angles of the proton and use energy and momentum conservation to eliminate all angles except θ_π and ϕ_π. This leads to a set of much simpler equations:

$$\sigma_0(\zeta)=a_{00}+b_{00}(3\cos^2\theta_\pi-1), \tag{10a}$$

$$\sigma_0(\zeta)A_{y0}(\zeta)=[a_{y0}\sin\theta_\pi+c_{y0}\sin 2\theta_\pi]\cos\varphi_\pi, \tag{10b}$$

$$\sigma_0(\zeta)A_\Sigma(\zeta)=a_\Sigma+b_\Sigma(3\cos^2\theta_\pi-1), \tag{10c}$$

$$\sigma_0(\zeta)A_{zz}(\zeta)=a_{zz}+b_{zz}(3\cos^2\theta_\pi-1), \tag{10d}$$

$$\sigma_0(\zeta)A_\Delta(\zeta)=a_\Delta\sin^2\theta_\pi\cos 2\varphi_\pi, \tag{10e}$$

$$\sigma_0(\zeta)A_{xz}(\zeta)=[a_{xz}\sin\theta_\pi+c_{xz}\sin 2\theta_\pi]\cos\varphi_\pi. \tag{10f}$$

The symbol ζ now represents the reduced set of variables $\{p_\pi,\theta_\pi,\phi_\pi\}$. These equations display a simple and characteristic ϕ_π dependence of the different polarization observables, and show the expected θ_π dependence. The coefficients $a_\nu,b_\nu,\dots$ for set (10) correspond to those in Eqs. (9). They are obtained by one- or two-parameter fits to the observed angular distributions, separately for each observable.

B. Extraction of polarization observables

The data analysis, as described in the previous sections, identifies the reaction particles, assesses the background for each spectrum, and calculates the kinematic variables and spin-dependent cross sections of the reaction products. It produces event files which contain kinematically complete information for all detected reaction particles. For each beam energy there are 12 such event files, one for each combination of beam and target spin. These yields are first corrected for the beam luminosity, which can vary for beam "spin-up" and "spin-down" subcycles, and for the background measurement. The background correction was made for each se-

lected θ_π angle bin individually. The ratios R_i of yields for different spin combinations, integrated over a chosen θ_π range, are then analyzed as a function of ϕ_π, because the allowed ϕ_π dependence can be predicted from spin coupling rules [21]. For this energy range, only final states with pn or pion angular momenta of 0 and 1 are expected to be significant. In a previous measurement of $pp\to d\pi^+$ at 400 MeV, it was found that any $l_\pi=2$ contribution is very small [30]. This allows us to consider only transitions to Ss, Sp, Ps, and Pp final states in the analysis. Sd and Ds transitions would affect the energy dependence of the coefficients only, and so are very difficult to separate from Pp transitions [26]. They will be ignored in this analysis. We then have explicit predictions for the expected θ and ϕ dependences from Eq. (10).

The combination of $p+\pi^+$ and $p+n$ measurements provides model-independent values for the polarization observables for all polar and azimuthal angles of the pion. The low neutron detection efficiency and the resulting low statistical accuracy of the $p+n$ data make it advisable to display the combined data using some theoretical guidance. As shown below, $A_\Sigma(\theta_\pi),A_\Delta(\theta_\pi)$, and $A_{zz}(\theta_\pi)$ must be symmetric about $\theta_\pi=90°$ for the transitions considered. So a good analysis in terms of the pion coordinates does not require the (redundant) data at large polar angles. This simplification, and the fact that all published theoretical predictions have been presented in terms of the pion coordinates, make these coordinates our preferred system for the analysis.

The microscopic relations between the coefficients and the transition amplitudes can be derived from the partial-wave expansion described in the Appendix of Ref. [26], but they are complicated. Moreover, the number of individual $pp\to pn\pi^+$ amplitudes contributing above 350 MeV has become too large (19 rather than 12 for $pp\to pp\pi^0$), since isospin 1 and 0 are present in the final state. They could not be deduced individually from the $pp\to pn\pi^+$ data available.

When calculating the value of a polarization observable from Eqs. (9) or (10), one evaluates the ratio $A_{ij}(\xi)=\sigma_0(\xi)A_{ij}(\xi)/\sigma_0(\xi)$, so the overall normalization of all terms in these equations cancels. As seen from Eqs. (10) the yield ratios $R_i(\phi_\pi)$ could either be constant or have a ϕ_π or $2\phi_\pi$ dependence. This is borne out by the data (compare Fig. 12).

The polarization observables were deduced by evaluating the observed ϕ_π dependences of the ratios R_i for selected beam and target spin combinations. This evaluation is complex when longitudinal as well as transverse beam polarizations are present at the same time. Therefore, the devolution process uses the computerized fitting routine BMW [31], which was written for this purpose.

Figure 12 shows the ϕ_π dependence of six spin-dependent yield ratios. The data for the beam (first arrow) and target spin combinations indicated have been integrated over all coordinates other than the coordinate ϕ_π. The curves are fits using one to three components of Eqs. (10). The first three rows present different ways to extract the analyzing power $A_y(\phi_\pi)$. The lower three rows contain information on $A_\Sigma=A_{xx}+A_{yy}$, $A_\Delta=A_{xx}-A_{yy}$, and contribu-

SPIN CORRELATIONS IN $\vec{p}\vec{p}\rightarrow pn\pi^+$ PION PRODUCTION . . .
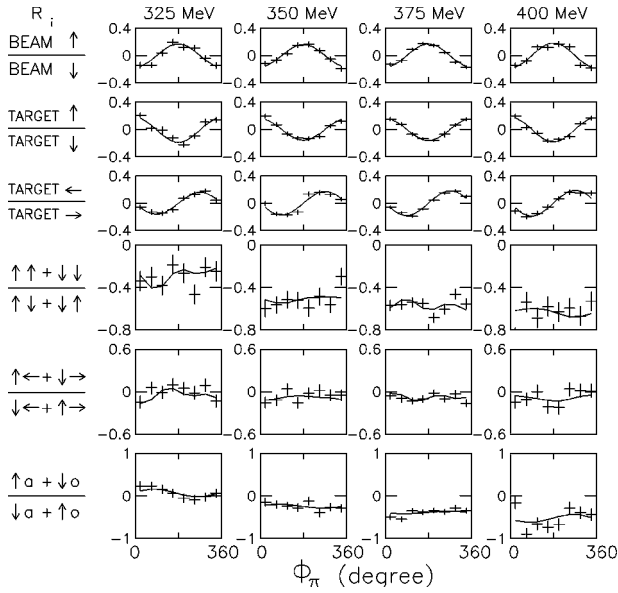
PHYSICAL REVIEW C **65** 024003

FIG. 12. The yield-related ratios $(R_i-1)/(R_i+1)$ as a function of the pion azimuthal angle ϕ_π for data integrated over all other coordinates. The specific beam and target spin combinations selected are listed on the left. For multiple arrows the orientation of the beam spin is shown first. Longitudinal polarization is indicated by the symbols o (opposite) and a (along the beam direction). The solid curves represent a least-square fit using the expected theoretical ϕ_π dependence.

tions from A_{zz} and A_{xz}. For some ratios the statistics are marginal, and one cannot exclude the potential presence of l components higher than included in the analysis, but the ϕ_π-dependent fits show that the inclusion of Ss, Sp, Ps, and Pp transitions is sufficient to reproduce the data within experimental errors.

For the simultaneous detection of neutrons and protons, our data sample the full range for θ_π, although with low statistics. We combine the $p+\pi$ and $p+n$ data sets to obtain optimal spin correlation coefficients for the full angular region. We avoid difficulties generated by the nonuniform detector acceptances in θ_π by evaluating the $p+n$ and $p+\pi$ relations $A_{ij}(\cos\theta_\pi)$, which are ratios of cross sections at a given angle. [Our detection efficiency does not depend on spin, and the detector acceptances cancel out for $A_{ij}(\cos\theta_\pi)$.] The combined $p+n$ and $p+\pi^+$ sets yield complete angular distributions with their best statistics at forward angles. The unpolarized angular distribution $\sigma_0(\theta_\pi)$ was obtained to sufficient accuracy from the $p+n$ branch. The angular distributions can now be integrated. To best account for experimental errors, we have chosen to integrate Eqs. (10) directly after the fitting coefficients are deduced.

Some of the polarization ratios measured are not independent, as the first three rows in Fig. 12 show. The reaction has additional redundancies. If parity is conserved and if we have identical particles in the entrance channel, this redundancy can give us back-angle information for A_y even though our detectors only cover forward polar angles for the direct detection of pions. The correlation we use repeatedly is

$$A_{ij}(\theta_p,\phi_p,\theta_\pi,\phi_\pi)=A_{ji}(\pi-\theta_p,\phi_p+\pi,\pi-\theta_\pi,\phi_\pi+\pi). \tag{11}$$

This relation holds for $i\neq j$ and also for $i=j$. That is, since both A_{xz} and A_{zx} are measured at forward angles, we will obtain the back angle information for A_{xz} from the A_{zx} measurement at forward angles. The polarization observables A_{xz} and A_{zx} are not symmetric about $\theta_\pi=90°$, so this redundancy becomes very useful.

V. RESULTS

A. Polarization observables

It follows from Eq. (11) that the observables A_Σ, A_Δ, and A_{zz} are symmetric about $\theta_\pi=90°$ ($\cos\theta_\pi=0$). Within statistical errors the experimental data agree with this expectation. In Fig. 13 we have reduced the scatter from the low statistics of the $p+n$ coincidences by combining the corresponding data for forward and backward polar angles. The data for $\cos\theta_\pi\geqslant0.5$ are dominantly determined by events from $p+\pi$ coincidences. In agreement with theoretical expectations, there is only a slow dependence on the polar angle, so the lack of good statistics near $\theta=90°$ does not impede comparison with theory or the extraction of good values for the integrated polarization observables.

Figure 14 shows results for $A_y(\theta_\pi)$ and $A_{xz}(\theta_\pi)$ for the full angular range, so potential asymmetries can be seen. The statistically most accurate data were obtained for 375 MeV. Here and at 400 MeV the Jülich model is at odds with the data. The fit with Eq. (10) (solid lines) does much better. Still, a close inspection of the fits shows some small, but statistically significant differences between the partial wave curve and the data at very small and very large angles. We also see from Table II that the χ^2 value for the A_y fit has become large. The A_y data suggest that higher partial waves enter at 375 MeV, but the experimental uncertainties discourage the extraction of relatively small contributions.

The fits obtained with Eq. (10) are good (i.e., $\chi^2\approx1$ for all curves except for A_y at 375 and 400 MeV). Therefore Eqs. (10) together with the coefficients of Table II can be used to represent the new data. The coefficients in these equations are bilinear sums of the reaction amplitudes. Their experimental values are given in Table II. This set is also used to obtain the integrated spin correlation coefficients. Integration of the angular distributions shown above produces the spin correlation coefficients in Cartesian coordinates. These coefficients were the original objective of this experiment. They are now known with good statistical accuracy, and are given in Table III. A comparison of these integrated polarization observables as a function of beam energy with predictions of the Jülich model is shown in Fig. 15.

For completeness we note that our attempt to extract noncoplanar angular distributions for A_{z0} produced only small negative values with large statistical errors (not shown). At 375 MeV our results are consistent with zero. They still agree with the $pp\rightarrow pp\pi^0$ results, provided we assume a negligible contribution for the isoscalar component.

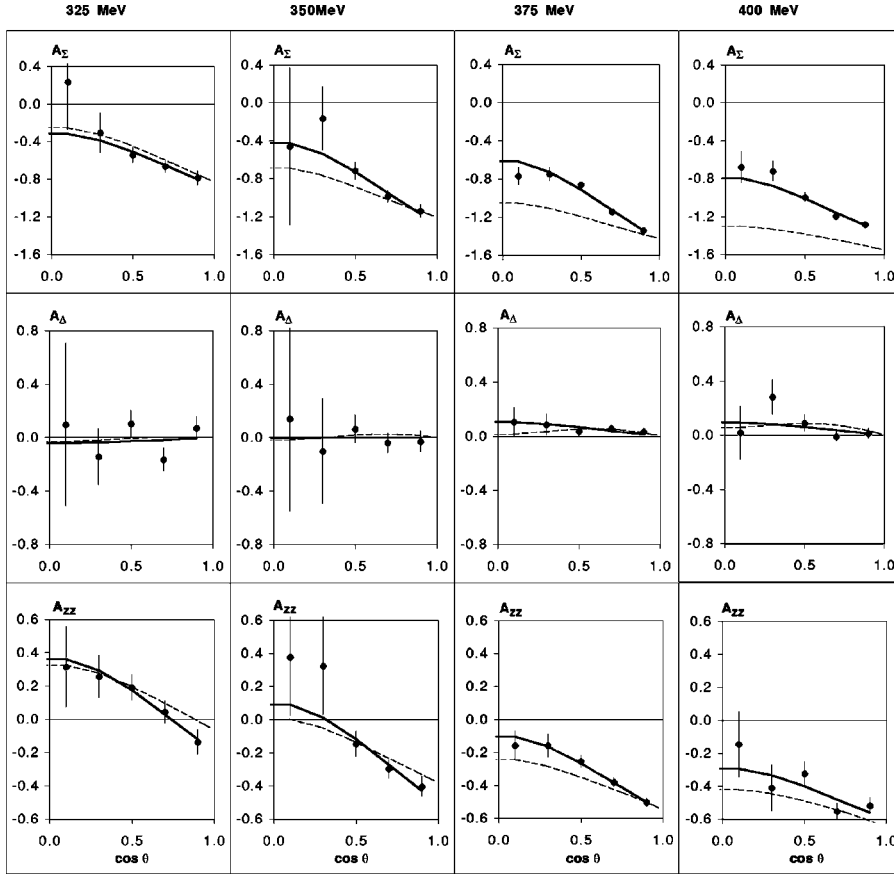It is clear from Figs. 13, 14, and 15 that the distributions

FIG. 13. θ_π dependence for the polarization observables $A_\Sigma \equiv A_{xx} + A_{yy}$, $A_\Delta \equiv A_{xx} - A_{yy}$, and A_{zz}, in Cartesian units. Data for the range $0.5 < \cos\theta < 1$ are primarily determined by the $p + \pi$ coincidences. The remaining points come from the $p + n$ coincidences. The error bars include all random errors as well as estimated uncertainties from background subtraction. The dashed lines are Jülich model predictions by Hanhart *et al.* [11]. The solid lines show fits with Eqs. (10).

based on the Jülich model are in good agreement with the data at 325 MeV. However, above $\eta = 0.7$ they produce ever larger χ^2 values when compared to the data. These disagreements become striking for A_Σ and A_y. The failures are most visible for A_y, an observable sensitive to admixtures of higher partial waves. (More serious disagreements with this model have been seen for the isovector production in $pp \rightarrow pp\pi^0$ [26]. However, as discussed below, in this energy region isovector terms contribute less than 10% to the $pp \rightarrow pn\pi^+$ cross section. The observed differences in $pp \rightarrow pn\pi^+$ grow well beyond this level.)

Our partial wave analysis, which includes Ss, Sp, Ps, and Pp transitions, generally provides fits to the measured angular distributions with χ^2 (per degree of freedom) values near 1. The exceptions are A_y at 375 and at 400 MeV, where the cross sections are largest and the statistics are good. Some χ^2 values as large as 3.9 are found if only statistical errors are considered.
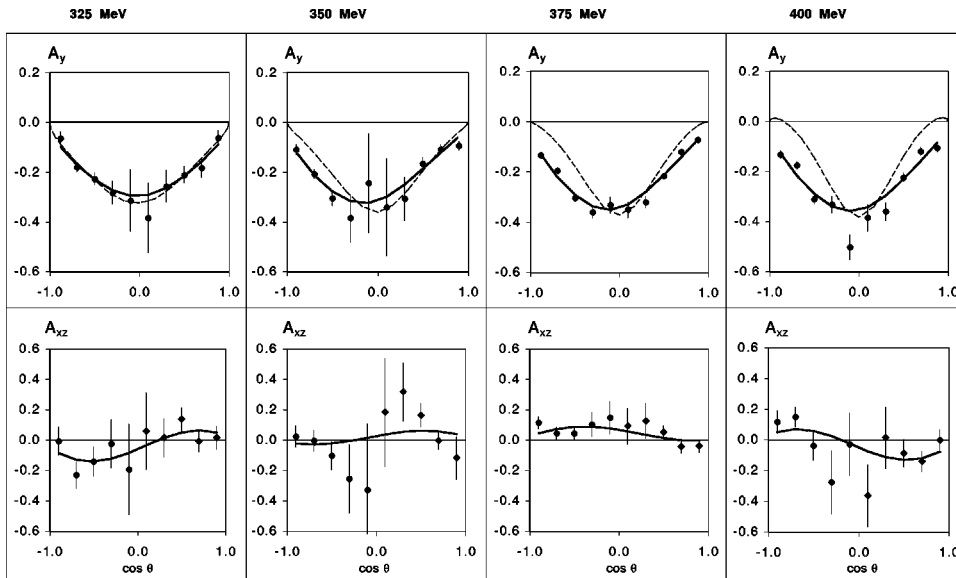

FIG. 14. θ_π dependence for the polarization observables A_y and A_{xz} in Cartesian units. The dashed lines are Jülich predictions. The solid lines show fits to the data using Eqs. (10).

TABLE II. Coefficients for the fits with Eqs. (10) that reproduce the measured angular distributions of the polarization observables. The associated Legendre polynomials used for the fits are determined by selection rules for Ss, Sp, Ps, and Pp transitions. The unpolarized angular distribution $\sigma_0(a_{00}, b_{00})$ is given in arbitrary units by setting $a_{00} = 1$. The errors listed refer to the individual fitting coefficients. The χ^2 numbers give the overall quality of the fit to the data per degree of freedom. The fits are shown in Figs. 11, 13, and 14.

Name	325 MeV param. value	param. error	χ^2 data	350 MeV param. value	param. error	χ^2 data	375 MeV param. value	param. error	χ^2 data	400 MeV param. value	param. error	χ^2 data
a_{00}	1	-	-	1	-	-	1	-	-	1	-	-
b_{00}	0.168	0.035	-	0.190	0.040	-	0.199	0.030	-	0.196	0.045	
a_Σ	-0.560	0.052	0.5	-0.810	0.055	0.6	-0.994	0.015	2.8	-1.070	0.024	1.4
b_Σ	-0.303	0.063		-0.478	0.067		-0.510	0.018		-0.439	0.029	
a_Δ	-0.037	0.091	1.4	-0.001	0.097	0.2	0.084	0.028	1.3	0.075	0.045	1.4
b_Δ	-	-	-	-	-	-	-	-	-	-	-	-
a_{zz}	0.120	0.042	0.1	-0.177	0.047	0.8	-0.310	0.018	1.0	-0.431	0.037	3.1
b_{zz}	-0.188	0.054		-0.257	0.057		-0.233	0.021		-0.199	0.043	
a_{y0}	-0.247	0.015	0.5	-0.255	0.013	0.9	-0.276	0.005	2.4	-0.285	0.008	3.9
c_{y0}	0.007	0.013		0.050	0.010		0.044	0.005		-0.032	0.007	
a_{xz}	-0.051	0.042	0.7	0.021	0.042	1.2	0.053	0.021	1.1	-0.041	0.041	1.2
c_{xz}	0.106	0.038		0.047	0.036		-0.040	0.020		-0.104	0.036	

The values for the product $P*Q$ are known to good precision (see Table I), but errors for the beam (P) or target (Q) polarization individually are not negligible at the lower energies. Changes in P and Q affect only the analyzing powers $A_y(\theta)$. They could reduce or increase the asymmetry of the angular distributions. Typically, the uncertainties in P are smaller than the statistical errors.

B. Discussion and comparison with other work

The statistical and fitting errors listed in Tables II and III include all known and estimated random errors. As explained above, all angles were measured simultaneously, and systematic normalization errors for A_{ij} are unlikely. Based on the detector design and redundant measurements, we expect that all systematic errors have remained small. In the center region ($\cos\theta \approx 0$) the angular distributions show large statistical errors. However, these data points do not materially affect the partial wave fits or the integrals. We note that our initial results reported in Ref. [19] were subject to some model dependence that is absent here. Nevertheless, they are consistent with the final results presented here. Noticeable asymmetries around 90° have been seen for A_y above 350

MeV. In the framework of our partial-wave analysis this asymmetry must be produced by Pp transitions. (At higher energies such asymmetries can also be produced by Ds and Sd transitions.) With the possible exception of the analyzing powers $A_y(\theta)$ at 375 and 400 MeV, the pion production data are well represented by the partial wave predictions based on the assumption of Ss, Ps, Sp, and Pp transitions. The Jülich model predictions and the data agree for A_Δ. However, we see serious disagreements for A_Σ and A_y as the beam energy increases. Reference [11] included more amplitudes than our analysis, but the calculations predicted little asymmetry for $A_y(\theta)$. The differences for A_y and the increasing divergence with energy are also seen in Fig. 15. At this time there are no predictions available for A_{xz} and A_{z0}.

C. Deduction of important partial waves

The number of contributing partial waves grows rapidly with energy. If we restrict ourselves to Ss, Sp, Ps, and Pp contributions as above, the 19 individual amplitudes listed in Table IV are needed for a detailed interpretation of the data. There are 12 isoscalar amplitudes and seven isovector amplitudes. The experimental information available includes the

TABLE III. Beam energy, the η parameter, and the deduced integrated spin correlation coefficients. The table gives the weighted average of all runs as shown in Fig. 15.

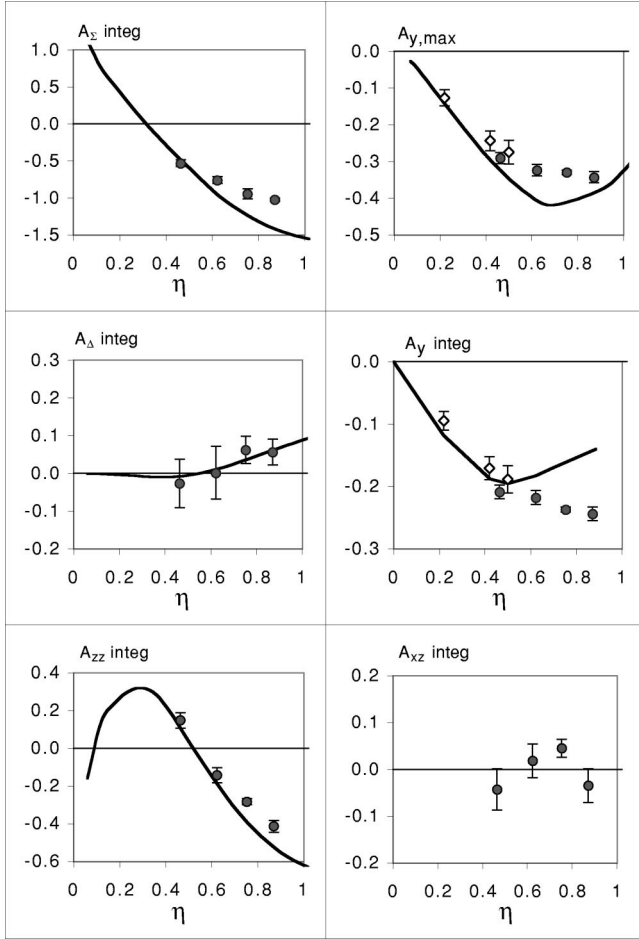| T (MeV)	η	$\overline{A_\Sigma}$	$\overline{A_\Delta}$	$\overline{A_{zz}}$	$\overline{A_{y0}}$	$\overline{A_{xz}}$
325.6	0.464	-0.533 ± 0.046	-0.027 ± 0.064	0.148 ± 0.041	-0.209 ± 0.011	-0.043 ± 0.044
350.5	0.623	-0.761 ± 0.046	0.001 ± 0.070	-0.143 ± 0.040	-0.218 ± 0.011	0.018 ± 0.036
375.0	0.753	-0.945 ± 0.068	0.062 ± 0.036	-0.283 ± 0.016	-0.237 ± 0.004	0.045 ± 0.019
400.0	0.871	-1.026 ± 0.023	0.056 ± 0.034	-0.414 ± 0.032	-0.244 ± 0.011	-0.035 ± 0.036

FIG. 15. Energy dependence of the integrated spin correlation coefficients $\overline{A_\Sigma}$, $\overline{A_\Delta}$, $\overline{A_{zz}}$ $\overline{A_{xz}}$, and $\overline{A_{y0}}$, and the peak analyzing power $A_{y,max}$ for $\vec{p}\vec{p}\rightarrow pn\pi^+$. The diamond shape symbols represent measurements at lower energies and are taken from Ref. [18]. The solid lines are predictions of the Jülich meson exchange model. (There is no prediction for A_{xz}.)

TABLE IV. Angular momentum quantum numbers for the partial waves of the reaction $pp\rightarrow pn\pi^+$.

Type		Label	$^{2s_i+1}l_J\rightarrow^{2s_f+1}l_p j,l_\pi$
Ss	isoscalar	a_1	$^3P_1\rightarrow^3S_1,s$
Ss	isovector	b_0	$^3P_0\rightarrow^1S_0,s$
Sp	isoscalar	a_0	$^1S_0\rightarrow^3S_1,p$
		a_2	$^1D_2\rightarrow^3S_1,p$
Ps	isovector	b_1	$^1S_0\rightarrow^3P_0,s$
		b_2	$^1D_2\rightarrow^3P_2,s$
Pp	isoscalar	a_3	$^3P_0\rightarrow^1P_1,p$
		a_4	$^3P_1\rightarrow^1P_1,p$
		a_5	$^3P_2\rightarrow^1P_1,p$
		a_6	$^3F_2\rightarrow^1P_1,p$
Pp	isovector	b_3	$^3P_0\rightarrow^3P_1,p$
		b_4	$^3P_2\rightarrow^3P_1,p$
		b_5	$^3P_2\rightarrow^3P_2,p$
		b_6	$^3F_2\rightarrow^3P_1,p$
		b_7	$^3F_2\rightarrow^3P_2,p$
		b_8	$^3P_1\rightarrow^3P_0,p$
		b_9	$^3P_1\rightarrow^3P_1,p$
		b_{10}	$^3P_1\rightarrow^3P_2,p$
		b_{11}	$^3F_3\rightarrow^3P_2,p$

terest. A suitable combination of the 19 partial cross sections into six groups allows us to find the Sp and Ps strengths separately to deduce the lowest Pp isoscalar partial cross section for the amplitude a_3 directly, and to put a close upper limit on the Ss contributions. We will identify the isoscalar partial wave cross sections by $\sigma(a_0)$, $\sigma(a_1)$, $\sigma(a_2)$, ... and the isovector partial wave cross sections by $\sigma(b_0)$, $\sigma(b_1)$, $\sigma(b_2)$, ... as in Table V. Generally, $\sigma(a_i) = C_i|a_i|^2$, where the C_i factor is a combination of factors like π and Clebsch-Gordan coefficients, which can differ from amplitude to amplitude. (Therefore, the partial cross sections listed in Table V do not provide the magnitude of the corresponding amplitudes without further work.) The notation $\sigma(a_1,a_{4\rightarrow6})$ implies that we could not separate the cross sections for a_1, the Ss component, from the Pp components a_4 to a_6. Hence $\sigma(a_1,a_{4\rightarrow6})\equiv\sigma(a_1)+\sigma(a_4)+\sigma(a_5)+\sigma(a_6)$. The partial cross section groups that could be isolated are given in Eqs. (12):

Sp isoscalar terms :

$$\sigma(a_0,a_2)=\frac{1}{8}(\Delta\sigma_L+2\Delta\sigma_T+2\sigma_{tot}-\Delta\sigma_L'-2\Delta\sigma_T'-2\sigma_{tot}'),$$
(12a)

Ps isovector terms:

$$\sigma(b_1,b_2)=\frac{1}{8}(\Delta\sigma_L'+2\Delta\sigma_T'+2\sigma_{tot}'),$$
(12b)

three cross sections σ_{tot}, $\Delta\sigma_T$, and $\Delta\sigma_L$ for $pp\rightarrow pn\pi^+$ that are related to these amplitudes. In addition a recent $pp\rightarrow pp\pi^0$ study provides the three relevant isovector cross sections σ_{tot}', $\Delta\sigma_T'$, and $\Delta\sigma_L'$ (Ref. [26], Table V). As long as isospin is a good quantum number these cross sections also give the isovector part of the $pp\rightarrow pn\pi^+$ reaction if taken at the same η. So one has six new measurements for 19 variables. This necessitates some restriction of the further analysis. In a previous $pp\rightarrow pn\pi^+$ study [18], closer to threshold, the partial-wave space was restricted to the lowest isoscalar amplitudes a_0,a_1,a_2, and to the lowest known isovector amplitudes. With this simplification and with reliance on the measured analyzing powers three amplitudes were deduced for $\eta\leq0.5$. Some of these earlier results will be shown below. It will become apparent in comparison with our data that the angular momentum space considered in Ref. [18] is too small for $\eta>0.3$. For $0.3<\eta<0.9$ it becomes necessary to consider all Ss, Sp, Ps, and Pp contributions. In order to reduce the number of variables we use similarities in the spin algebra coefficients for the 19 amplitudes of in-

TABLE V. Listing of the $pp\rightarrow pn\pi^+$ partial-wave strengths for the groups of isoscalar and isovector amplitudes indicated. The 300-MeV results listed were taken from Ref. [18]. The 300-MeV strengths not listed are assumed to be negligible.

Isoscalars

E (MeV)	η	$Sp(a0,a2)$	error	$Ss+Pp$ $(a1,a4-6)$	error	$Pp(a3)$	error
300	0.220	0.088	0.030	0.740	0.050	-	-
325.6	0.464	0.342	0.018	0.570	0.024	0.006	0.018
350.5	0.623	0.469	0.018	0.421	0.023	0.052	0.018
375	0.753	0.541	0.020	0.342	0.011	0.050	0.020
400	0.871	0.579	0.013	0.262	0.019	0.063	0.013

Isovectors

E (MeV)	η	$Ps(b1,b2)$	error	$Ss+Pp$ $(b0,b3)$	error	$Pp(b4-11)$	error
300	0.220	-	-	0.173	0.022	-	-
325.6	0.464	0.007	0.002	0.073	0.007	0.004	0.003
350.5	0.623	0.014	0.003	0.044	0.005	0.007	0.002
375	0.753	0.019	0.002	0.034	0.003	0.016	0.002
400	0.871	0.024	0.003	0.034	0.004	0.031	0.004

$Ss+Pp$ isoscalar terms:

$$\sigma(a_1,a_{4\rightarrow6})=\frac{1}{4}(-\Delta\sigma_L+2\sigma_{tot}+\Delta\sigma'_L-2\sigma'_{tot}),$$

(12c)

$Ss+Pp$ isovector terms:

$$\sigma(b_0,b_3)=\frac{1}{8}(\Delta\sigma'_L-2\Delta\sigma'_T+2\sigma'_{tot}),$$ (12d)

Pp isoscalar terms:

$$\sigma(a_3)=\frac{1}{8}(\Delta\sigma_L-2\Delta\sigma_T+2\sigma_{tot}-\Delta\sigma'_L+2\Delta\sigma'_T-2\sigma'_{tot}),$$

(12e)

Pp isovector terms: $\quad\sigma(b_{4\rightarrow11})=\frac{1}{4}(-\Delta\sigma'_L+2\sigma'_{tot}).$

(12f)

Of these six equations, which hold for $pp\rightarrow pn\pi^+$, three also hold for $pp\rightarrow pp\pi^0$. We note that Eq. (12b) has been presented before. It is identical to Eq. (13) in Ref. [26]. The six equations now permit a calculation of partial wave cross sections to the specified groups of final states from the measured spin-dependent cross sections. The sum of these partial cross sections equals the total π^+ production cross section. Since the partial cross sections add incoherently the effect of higher lying weak amplitudes is minimized. This is an advantage over relying on analyzing powers, which are sensitive to even small admixtures. The amplitudes included in each group are indicated on the left side of Eqs. (12).

In many experiments, including the present one, it is much easier to measure accurate cross section ratios than absolute cross sections. So our experimental $pp\rightarrow pn\pi^+$ quantities are given as a fraction of the total π^+ production cross section σ_{tot}. Equations (12) are easily rewritten in terms of partial wave strengths by dividing both sides by

σ_{tot}. For the $p+\pi^+$ branch the values $\Delta\sigma_T/\sigma_{tot}$ and $\Delta\sigma_L/\sigma_{tot}$ were calculated from Eqs. (7) and $A_\Sigma(\theta)$, $A_\Delta(\theta)$, and $\sigma_0(\theta)$. In figures and tables we will generally use the ratios of partial-wave cross sections to total cross sections. We refer to them as partial-wave strengths.

For use in this study the total $pp\rightarrow pp\pi^0$ and $pp\rightarrow pn\pi^+$ cross sections were taken from the literature and interpolated for the present η values. We obtained the $pp\rightarrow pp\pi^0$ information needed from Ref. [26] and the $pp\rightarrow pn\pi^+$ total cross sections from Ref. [18] and from Fig. 2 in Ref. [6]. The accuracy of the total cross section ratios so obtained is not very high, but it will suffice here because the isoscalar terms of interest are an order of magnitude larger than the isovector terms. The partial cross section strengths derived with Eqs. (12) are displayed in Fig. 16 and listed in Table V.

The primed cross sections are the (pure isovector) cross sections measured for $pp\rightarrow pp\pi^0$, which are also more accurately given as fractional strengths. To work in terms of $pp\rightarrow pn\pi^+$ partial wave strengths the $pp\rightarrow pp\pi^0$ strengths of Ref. [26] have to be multiplied by the ratio of the $pp\rightarrow pp\pi^0$ and $pp\rightarrow pn\pi^+$ unpolarized cross sections, taken at the same relevant η values.

Figure 16 shows the change of partial wave strength with energy for Sp, Ps, and other groups. It is immediately apparent that for the energy region studied the leading isoscalar partial cross sections are an order of magnitude larger than the isovector ones. It helps our discussion that lowest-lying Pp isoscalar partial wave strength $Pp(a_3)$ could be resolved. It is much smaller than the Ss and Sp strengths. So is the sum of all isovector cross sections for b_4 to b_{11}. The Pp strengths attributable to b_3 can be assessed by comparing $Pp(b_{4\rightarrow11})$ from this work with the heavy dash-dotted curve derived from Ref. [26] for the full Pp isovector strength $Pp(b_{3\rightarrow11})$.

Therefore, it seems reasonable to assume that the Pp contributions from a_4, a_5, a_6, and b_3, which could not be dis-
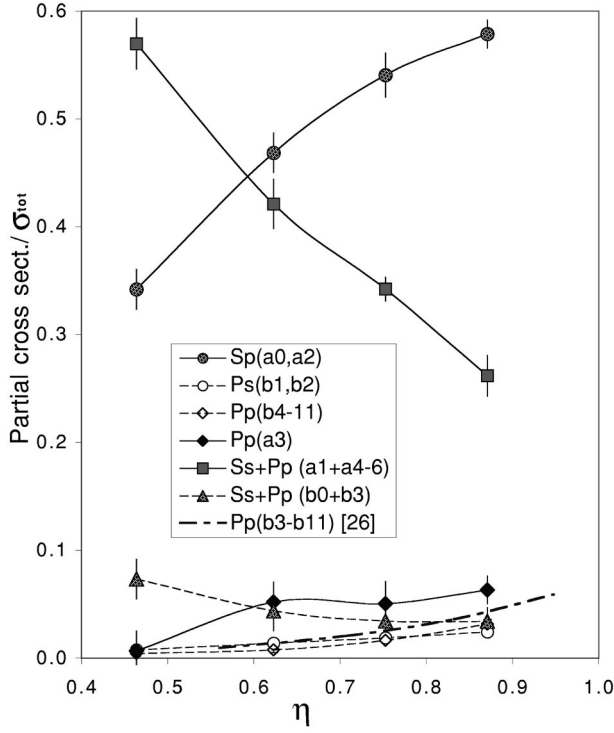
FIG. 16. Partial-wave strengths for six groups of amplitudes as function of η. The isoscalar cross sections are connected by solid lines, the isovector ones by dashed lines. The contributing amplitudes, including the (small) Pp contributions not resolved from the dominant Ss cross sections are indicated in the legend. The dash-dotted line represents the full Pp isovector strength contribution in $pp \rightarrow pn\pi^+$, as derived from the results of Ref. [26].

FIG. 17. Sums of isoscalar and isovector partial wave strengths as function of η. The $Sp+Ps$ sum is measured directly. The points labeled "Ss max" represent a close upper limit to the sum of the Ss partial cross sections. Any correction for the unresolved Pp amplitudes (a_4, a_5, and b_3) would lower the Ss curve (as indicated by the estimated errors). The admixtures can be expected to be smaller than $Pp(a_3)$. The lower points show the documented Pp strengths only. The data at $\eta=0.22$ and 0.42 are from Ref. [18].

entangled from the the Ss amplitudes, are also much smaller than the Ss terms. On this basis we estimate that they make up no more than 5–10 % of the "Pp entangled" Ss_{max} cross-section curve. For $\eta=0.9$ the $Sp(a_0,a_2)$ cross section has become dominant. As seen in Fig. 16, it is very much larger than the Ps isovector contribution. It would be of interest to resolve the isoscalar component a_0, because it can be used to constrain the strength of three-body forces [13]. However, in this analysis a_0 and the much larger amplitude a_2 always appear together. The Ss fraction, including the unresolved Pp contributions, has fallen to less than 0.3. This is consistent with the work at 420 MeV [32].

In Fig. 17 the data points give the summed $Sp+Ps$ strengths, the upper limit for the summed Ss strengths, and a lower limit for the Pp strength. The heavy dashed curve shows the likely energy dependence of the actual Ss strength. The divergence of the old and new $pp \rightarrow pn\pi^+$ interpretation near $\eta \approx 0.45$ serves as a reminder that a partial wave analysis is only model independent if it fully encompasses all contributing amplitudes. This apparently was no longer true for the 320 MeV data ($\eta=0.42$) of Ref. [18].

In this respect our present difficulty to perfectly reproduce A_y at 375 and 400 MeV in the Ss, Sp, Ps, and Pp frameworks (see Table II) should be taken as a warning. At these energies some higher partial waves may contribute enough
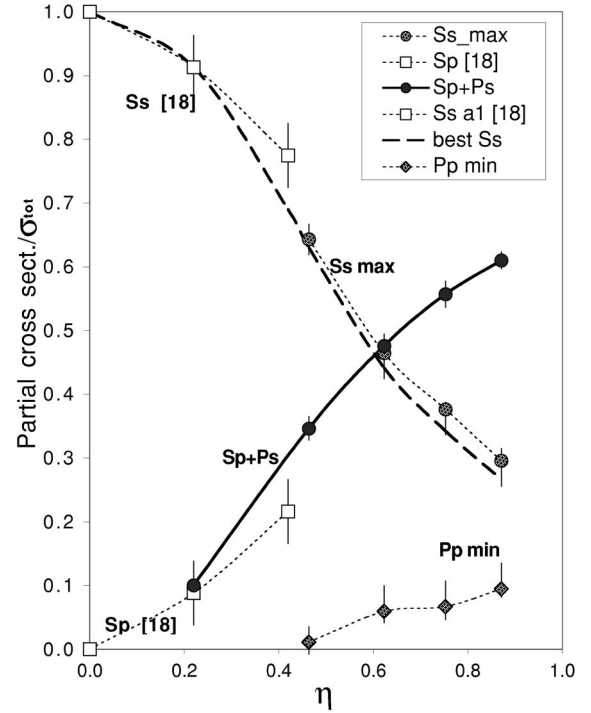
so that they must be considered, at least for the analyzing powers.

VI. CONCLUSIONS

We have measured the spin correlation coefficients $A_\Sigma = A_{xx}+A_{yy}$, $A_\Delta = A_{xx}-A_{yy}$, A_{zz}, A_{xz}, and A_y, as well as angular distributions for $\sigma(\theta_\pi)$ and the polarization observables $A_{ij}(\theta_\pi)$ at energies from 325 to 400 MeV. At the lowest energies the results are in agreement with prediction of the Jülich meson exchange model. The agreement deteriorates considerably at energies where Ss transitions no longer dominate. At 375 and 400 MeV some physics aspects in $\vec{p}\vec{p} \rightarrow pn\pi^+$ apparently are missed by the model. This suspicion is supported by the even poorer agreement of the model with the $\vec{p}\vec{p} \rightarrow pp\pi^0$ data [26].

The $pp \rightarrow pp\pi^0$ and $pp \rightarrow pn\pi^+$ reactions are found to differ greatly in the relative importance of Sp, Ps, and Pp transitions. Sp strongly feeds the delta resonance in $pp \rightarrow pn\pi^+$, but this transition is forbidden for $\vec{p}\vec{p} \rightarrow pp\pi^0$. By contrast, Ps contributions in $pp \rightarrow pn\pi^+$ are no larger than Pp contributions, as seen in Fig. 16. In $\vec{p}\vec{p} \rightarrow pn\pi^+$ the Ss and Sp isoscalar terms are most important while the Pp transitions just begin to contribute. For $\vec{p}\vec{p} \rightarrow pp\pi^0$ Pp becomes dominant at $\eta=0.7$.

The partial wave analysis was able to reproduce almost all polarization observables within experimental errors. This supports the postulated adequacy of considering only Ss, Sp, Ps, and Pp transitions in the near-threshold region. However, this angular momentum space may not be adequate to explain details of analyzing powers, because they can be affected by small admixtures of higher-lying transitions. Even in this limited space the number of individual partial waves for $\vec{p}\vec{p}\rightarrow pn\pi^+$ at 400 MeV is too large to deduce all individual amplitudes. Some interesting sum rules for groupings of amplitudes were found [Eqs. (12)], and the corresponding partial cross sections could be extracted. They show, e.g., that for $\eta < 1$ Pp and Ps terms play a considerably smaller role in $pp\rightarrow pn\pi^+$ than in $pp\rightarrow pp\pi^0$.

Further progress may come from improved theoretical models that can accurately predict the new data at hand. It is interesting to note again that the Jülich model does well at 325 MeV where Ss dominates, but it increasingly fails for $pp\rightarrow pn\pi^+$ (as well as for $pp\rightarrow pp\pi^0$) as higher angular momenta become important.

[1] M. Gell-Mann and K. M. Watson, Annu. Rev. Nucl. Sci. **4**, 219 (1954).

[2] A. H. Rosenfeld, Phys. Rev. **96**, 130 (1954).

[3] D. Koltun and A. Reitan, Phys. Rev. **141**, 1413 (1966).

[4] M. E. Schillaci, R. R. Silbar, and J. E. Young, Phys. Rev. **179**, 1539 (1969).

[5] H. O. Meyer *et al.*, Phys. Rev. Lett. **65**, 2846 (1990); also see, H. O. Meyer *et al.*, Nucl. Phys. **A539**, 633 (1992).

[6] W. W. Daehnick, S. A. Dytman, J. G. Hardie, W. K. Brooks, R. W. Flammang, L. Bland, W. W. Jacobs, T. Rinckel, P. V. Pancella, J. D. Brown, and E. Jacobsen, Phys. Rev. Lett. **74**, 2913 (1995).

[7] C. Hanhart, J. Haidenbauer, A. Reuber, C. Schutz, and J. Speth, Phys. Lett. B **358**, 21 (1995).

[8] C. Hanhart, Ph.D. thesis, University of Bonn, 1997.

[9] C. Hanhart, J. Haidenbauer, M. Hoffmann, U.-G. Meissner, and J. Speth, Phys. Lett. B **424**, 8 (1998).

[10] C. Hanhart, J. Haidenbauer, O. Krehl, and J. Speth, Phys. Lett. B **444**, 25 (1998).

[11] C. Hanhart, J. Haidenbauer, O. Krehl, and J. Speth, Phys. Rev. C **61**, 064008 (2000), and references therein.

[12] T.-S. H. Lee and D. O. Riska, Phys. Rev. Lett. **70**, 2237 (1993).

[13] C. Hanhart, U. van Kolck, G. A. Miller, Phys. Rev. Lett. **85**, 2905 (2000).

[14] C. A. da Rocha, G. A. Miller, and U. van Kolck, Phys. Rev. C **61**, 034613 (2000).

[15] B. Blankleider and A. N. Kvinikhidze, Few-Body Syst., Suppl. **12**, 223 (2000).

[16] J. G. Hardie, S. A. Dytman, W. W. Daehnick, W. K. Brooks, R. W. Flammang, L. C. Bland, W. W. Jacobs, P. V. Pancella, T. Rinckel, J. D. Brown, and E. Jacobson, Phys. Rev. C **56**, 20 (1997).

[17] W. W. Daehnick, R. W. Flammang, S. A. Dytman, D. J. Tedeschi, R. A. Thompson, T. Vrana, C. C. Foster, J. G. Hardie, W. W. Jacobs, T. Rinckel, E. J. Stephenson, P. V. Pancella, and W. K. Brooks, Phys. Lett. B **423**, 213 (1998).

[18] R. W. Flammang, W. W. Daehnick, S. A. Dytman, D. J. Tedeschi, R. A. Thompson, T. Vrana, C. C. Foster, J. G. Hardie, W. W. Jacobs, T. Rinckel, E. J. Stephenson, P. V. Pancella, and W. K. Brooks, Phys. Rev. C **58**, 916 (1998).

[19] Swapan K. Saha, W. W. Daehnick, R. W. Flammang, J. T. Balewski, H. O. Meyer, R. E. Pollock, B. v. Przewoski, T. Rinckel, P. Thörngren-Engblom, B. Lorentz, F. Rathmann, B. Schwartz, T. Wise, and P. V. Pancella, Phys. Lett. B **461**, 175 (1999).

[20] H. O. Meyer, L. D. Knutson, J. T. Balewski, W. W. Daehnick, J. Doskow, W. Haeberli, B. Lorentz, R. E. Pollock, P. V. Pancella, B. v. Przewoski, F. Rathman, T. Rinckel, Swapan K. Saha, B. Schwartz, P. Thörngren-Engblom, A. Wellinghausen, and T. Wise, Phys. Lett. B **480**, 7 (2000).

[21] L. D. Knutsen, in *Proceedings of the 4th International Conference on Nuclear Physics at Storage Rings, Indiana*, 1999, edited by H. O. Meyer and P. Schwandt, AIP Conf. Proc. No. 512 (AIP, Melville, NY, 2000), p. 177.

[22] T. Rinckel, P. Thörngren-Engblom, H. O. Meyer, J. T. Balewski, J. Doskow, R. E. Pollock, B. v. Przewoski, F. Sperisen, W. W. Daehnick, R. W. Flammang, Swapan K. Saha, W. Haeberli, B. Lorentz, F. Rathmann, B. Schwartz, T. Wise, and P. V. Pancella, Nucl. Instrum. Methods Phys. Res. A **439**, 117 (2000).

[23] T. Wise, A. D. Roberts, and W. Haeberli, Nucl. Instrum. Methods Phys. Res. A **336**, 410 (1993). Also see J. S. Price and W. Haeberli, *ibid.* **349**, 321 (1994).

[24] M. A. Ross *et al.*, Nucl. Instrum. Methods Phys. Res. A **344**, 307 (1994).

[25] B. v. Przewoski *et al.*, Phys. Rev. C **58**, 1897 (1998).

[26] H. O. Meyer, A. Wellinghausen, J. T. Balewski, J. Doskow, R. E. Pollock, B. von Przewoski, T. Rinckel, P. Thörngren-Engblom, L. D. Knutson, W. Haeberli, B. Lorentz, F. Rathmann, B. Schwartz, T. Wise, W. W. Daehnick, Swapan K. Saha, and P. V. Pancella, Phys. Rev. C **63**, 064002 (2001).

[27] W. W. Daehnick, W. K. Brooks, Swapan K. Saha, and D. O. Kreithen, Nucl. Instrum. Methods Phys. Res. A **320**, 290 (1992).

[28] A. Del Guerra, Nucl. Instrum. Methods **135**, 337 (1976).

[29] B. Morton, E. E. Gross, E. V. Hungerford, J. J. Malanify, and A. Zucker, Phys. Rev. **169**, 825 (1968).

[30] B. v. Przewoski, J. T. Balewski, J. Doskow, H. O. Meyer, R. E. Pollock, T. Rinckel, P. Thörngren-Engblom, A. Wellinghausen, W. Haeberli, B. Lorentz, F. Rathmann, B. Schwartz, T. Wise, W. W. Daehnick, Swapan K. Saha, and P. V. Pancella, Phys. Rev. C **61**, 064604 (2000).

[31] The computer code BMW was written by J. T. Balewski, H. O. Meyer, and A. Wellinghausen (unpublished).

[32] R. G. Pleydon, W. R. Falk, M. Benjamintz, S. Yen, P. L. Walden, R. Abegg, D. Hutcheon, C. A. Miller, M. Hartig, K. Hicks, G. V. O'Rielly, and R. Shyam, Phys. Rev. C **59**, 3208 (1999).